The Wintertime Water Mass Formation in the Northern Arabian Sea: A Model Study

T. G. PRASAD AND M. IKEDA

Division of Ocean and Atmospheric Sciences, Graduate School of Environmental Earth Science, Hokkaido University, Sapporo, Japan

ABSTRACT

Using a level 2 one-dimensional turbulent closure model, the evolution of the Arabian Sea High Salinity Water mass (ASHSW) has been studied. Model-derived heat fluxes, sea surface temperature (SST), and mixed layer depths (MLD) are found to be in reasonable agreement with the observations. Winter cooling is characterized by a net heat loss of 40 W m^{-2} from the ocean, while there is a mild heat loss in summer. Wind-driven turbulent mixing is considerably stronger than buoyancy forcing during the summer monsoon and explains the mechanism for governing deep MLD and cool SST. During winter, a large latent heat release by the ocean due to prevailing dry air from the north, together with reduced solar radiation and increased longwave radiation due to lower cloudiness, decreases the net heat flux considerably. Negative buoyancy flux plays a major role in the formation of ASHSW during winter, while kinetic energy-driven vertical mixing is relatively weaker than during the summer monsoon. A sensitivity test has confirmed that the humidity plays an important role in the heat budget of the northern Arabian Sea during winter.

1. Introduction

In the northern Arabian Sea, excess evaporation over precipitation during a relatively calm period of the winter monsoon is known to be responsible for the convective formation of the warm and high salinity Arabian Sea High Salinity Water mass (ASHSW; Prasanna Kumar and Prasad 1999). It was first documented by Rochford (1964) and subsequently by Morrison (1997). ASHSW starts forming in the northern Arabian Sea during November when the ocean begins to release heat. It subducts in the region north of 20°N and spreads equatorward along the $\sigma_t = 24$ isopycnal surface. The characteristics of this water mass are temperature, salinity, and depth ranges of 28°–24°C, 36.7–35.3 psu, and 0–100 m, respectively [for details see Prasanna Kumar and Prasad (1999)].

The core of the ASHSW shows pronounced spatiotemporal variability associated with seasonally reversing surface circulation (Morrison 1997; Rochford 1964; Prasanna Kumar and Prasad 1999). During the northeast Monsoon, the North Equatorial Current (NEC) advects warm and low salinity Bay of Bengal water into the Arabian Sea. The NEC bifurcates at the southern tip of India with a branch flowing along the west coast of India as a West India Coastal Current (WICC; Shetye et al. 1991). The eastern extent of the ASHSW is limited by the northward-flowing WICC. Lateral mixing with the Bay of Bengal water along the west coast of India and in the region south of 10°N during winter reduces its core salinity. The southward spreading of ASHSW is limited by the westward- (eastward) flowing NEC (Indian Monsoon Current) during the winter (summer) monsoon. During summer, the northward-flowing Somali Current along the western Arabian Sea contributes to limiting the southward spreading of ASHSW. Recent results (Fischer 2000; Lee et al. 2000) indicate that wind-driven turbulent mixing is considerably stronger than Ekman pumping (proposed by Bauer et al. 1991) in the Arabian Sea during summer monsoon. Northwest of the Findlater Jet (Findlater 1969), Ekman pumping partially counters wind-driven mixing causing a shallow ASHSW core, while southeast the two processes act together to deepen the ASHSW core.

In the equatorial region, the water mass can be found as a well-defined subsurface salinity maximum at about 100 m. Figure 1 shows vertical distribution of salinity along the equator during March and April (Levitus and Boyer 1994). The core of ASHSW stretching eastward below the equatorial low salinity water coincides with the boundary between the surface mixed layer and the stratified thermocline. This water mass capped over a stratified thermocline broadly determines the downward extent of fluxes of momentum, heat, and freshwater in the equatorial region. While there is definitely a link between salinity stratification and development of a warm pool in the southeastern Arabian Sea (Shenoi et al. 1999; Rao and Sivakumar 1999), a clear understanding of the evolution of this water mass would be an

Corresponding author address: T. G. Prasad, Division of Ocean and Atmospheric Sciences, Graduate School of Environmental Earth Science, Hokkaido University, N-10, W-5, Sapporo 060 0810, Japan. E-mail: tgprasad@ees.hokudai.ac.jp
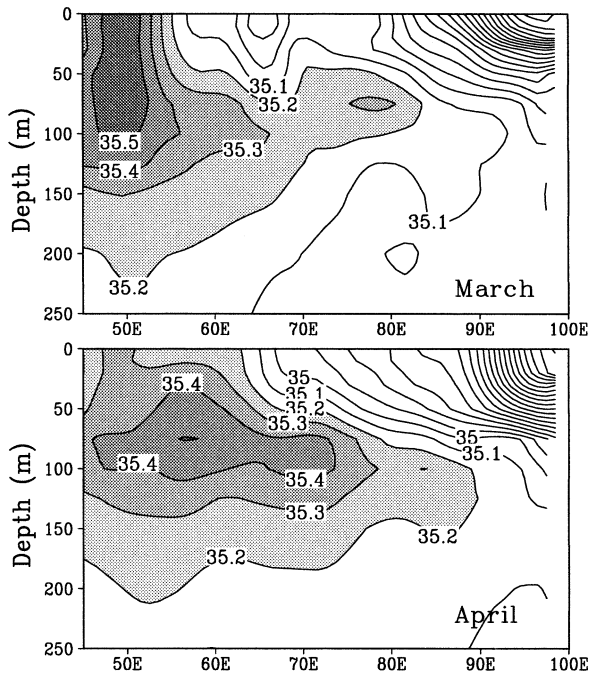
FIG. 1. Vertical distribution of salinity along the equator during (top) Mar and (bottom) Apr. The contour interval is 0.1 psu. Salinities >35.2 psu are shaded to demarcate the ASHSW. Note the eastward spreading of ASHSW below the low-salinity equatorial water.

important prerequisite for an improved prediction of the coupled monsoon–Indian Ocean system.

Much early work on modeling the mixed layer depth (MLD) and sea surface temperature (SST) variability in the Arabian Sea (e.g., Shetye 1986; Molinari et al. 1986; Rao 1986) are based on Kraus–Turner entrainment thermodynamics in which entrainment is caused by the surface production of turbulent energy (Kraus and Turner 1967). However, their objectives were to delineate the various dynamical processes responsible for the mixed layer development and SST variability. None of the above studies have addressed the formation of ASHSW.

The application of a 1D model in the Arabian Sea, where changes in surface forcing trigger Ekman convergence/divergence, and ignoring planetary wave motions and advection, may appear untenable. Nevertheless, in the present study we will use a one-dimensional second-order level 2 turbulent closure model to identify and isolate the possible mechanisms leading to the formation of the Arabian Sea High Salinity Water mass in the northern Arabian Sea. The strategy is to simulate the observed characteristics of ASHSW in the northern Arabian Sea. Our hypothesis is that the horizontal advection plays a negligible role in water mass formation in the northern Arabian Sea during winter, particularly within its core region. This assumption is not an unreasonable one for the process under study, because the wind-driven current is weak during this time. In the coastal regions, the role of advection, which is more important during the southwest monsoon, cannot be

ruled out. However, our aim is to simulate the observed characteristics of the ASHSW in the region far from the effect of both horizontal and vertical advection during winter. Indeed, it is important to keep in mind the limitations of a 1D model that can only track the response to changes in local forcing conditions in interpreting the results presented below. Nevertheless, the simulations below exhibit considerable skill in reproducing the basic details of the water mass formation in the northern Arabian Sea. We begin with a description of the model equations in section 2 followed by presentation and discussion of the model results in sections 3 and 4, respectively. We conclude with our major findings in this study and the limitations of the model in representing the winter water mass formation with possible clues to provide further improvement in ocean modeling.

2. The model equations

Time dependent one-dimensional momentum, temperature, and salinity equations are (Mellor and Durbin 1975; Ikeda 1986),

$$\frac{\partial U}{\partial t} - fV = \frac{\partial}{\partial z}\left(lqS_m\frac{\partial U}{\partial z}\right) \tag{1a}$$

$$\frac{\partial V}{\partial t} + fU = \frac{\partial}{\partial z}\left(lqS_m\frac{\partial V}{\partial z}\right) \tag{1b}$$

$$\frac{\partial T}{\partial t} = \frac{\partial}{\partial z}\left(lqS_h\frac{\partial T}{\partial z}\right) \tag{1c}$$

$$\frac{\partial S}{\partial t} = \frac{\partial}{\partial z}\left(lqS_h\frac{\partial S}{\partial z}\right), \tag{1d}$$

where U and V are the two components of mean horizontal velocity; T and S are mean temperature and salinity, respectively; z is a vertical coordinate, t is the time, f is the Coriolis parameter, l is the mixing length, q is the turbulent kinetic energy, and S_h and S_m are stability factors (since the turbulent closure model has been extensively used, detailed derivation of the model equations are presented in appendix A).

a. Boundary conditions

The boundary conditions at the air–sea interface are determined from the momentum, heat, and freshwater fluxes. The wind stress (τ_x, τ_y) at the air–sea interface gives

$$\rho_o lqS_m\left(\frac{\partial U}{\partial z}, \frac{\partial V}{\partial z}\right) = (\tau_x, \tau_y), \tag{2a}$$

where $\rho_o = 10^3$ kg m^{-3} is the water density.

The heat flux balance yields

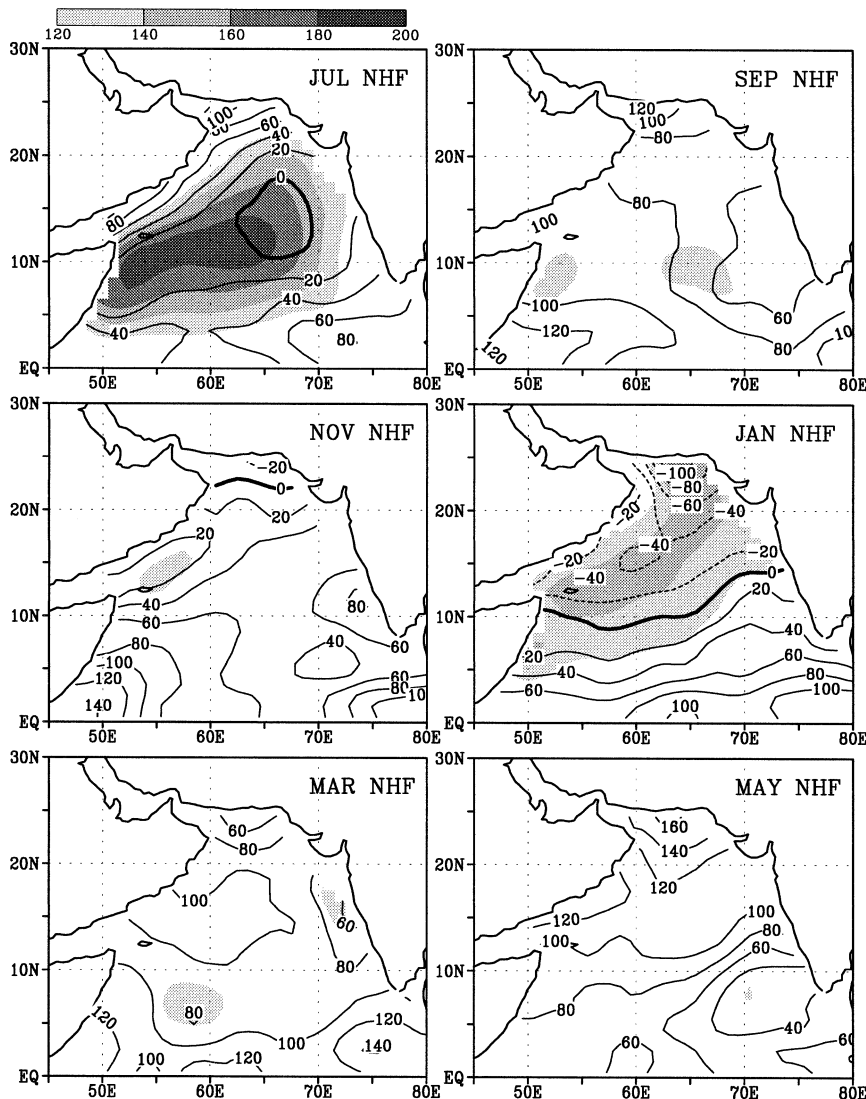$$\rho_o C_p lqS_h\frac{\partial T}{\partial z} = Q, \tag{2b}$$

FIG. 2. Bimonthly net heat flux in W m^{-2} obtained from the model (Jul–May). The contour interval is 20 W m^{-2}. Shaded region indicates the model-derived latent heat flux values at 20 W m^{-2} intervals between 120 and 200 W m^{-2}. The elevated latent heat flux due to dry air emanating from north leads to a net heat loss from the ocean (-40 W m^{-2}) in winter.

where $C_p = 4.2 \times 10^3$ J K^{-1} is the specific heat and Q is the net heat flux at the surface. Similarly the salt balance equation becomes

$$\rho_o l q S_h \frac{\partial S}{\partial z} = S(E - P), \qquad (2c)$$

where $E - P$ is the freshwater flux (evaporation–precipitation).

b. Forcing fields

The monthly mean data from the Southampton Oceanography Centre (SOC) for the period 1980–93 (Josey et al. 1999) are used to determine the forcing field Q, and 12-h wind from the ECMWF data during the year 1995 are used for the computation of wind stress (τ). Since we use one year of data, it is assumed that the particular year represents the normal year in the tropical Indian Ocean (see Weller et al. 1998; Lee et al. 2000). The 12-h sampling allows a realistic simulation of mixed layer characteristics. Since wind forcing is crucial to a turbulent closure model, such daily sampling is required for a realistic simulation. To calculate the forcing functions, we used SOC climatology monthly values of incoming solar radiation, the air temperature T_a, the relative humidity h_m, fractional cloudiness (C), and the vector wind $\mathbf{V}$ fields from the European Centre for Medium-Range Weather Forecasts (ECMWF). Note that we use model SST (T_m) to compute sensible Q_s and latent Q_l in the model; that is, the model develops its
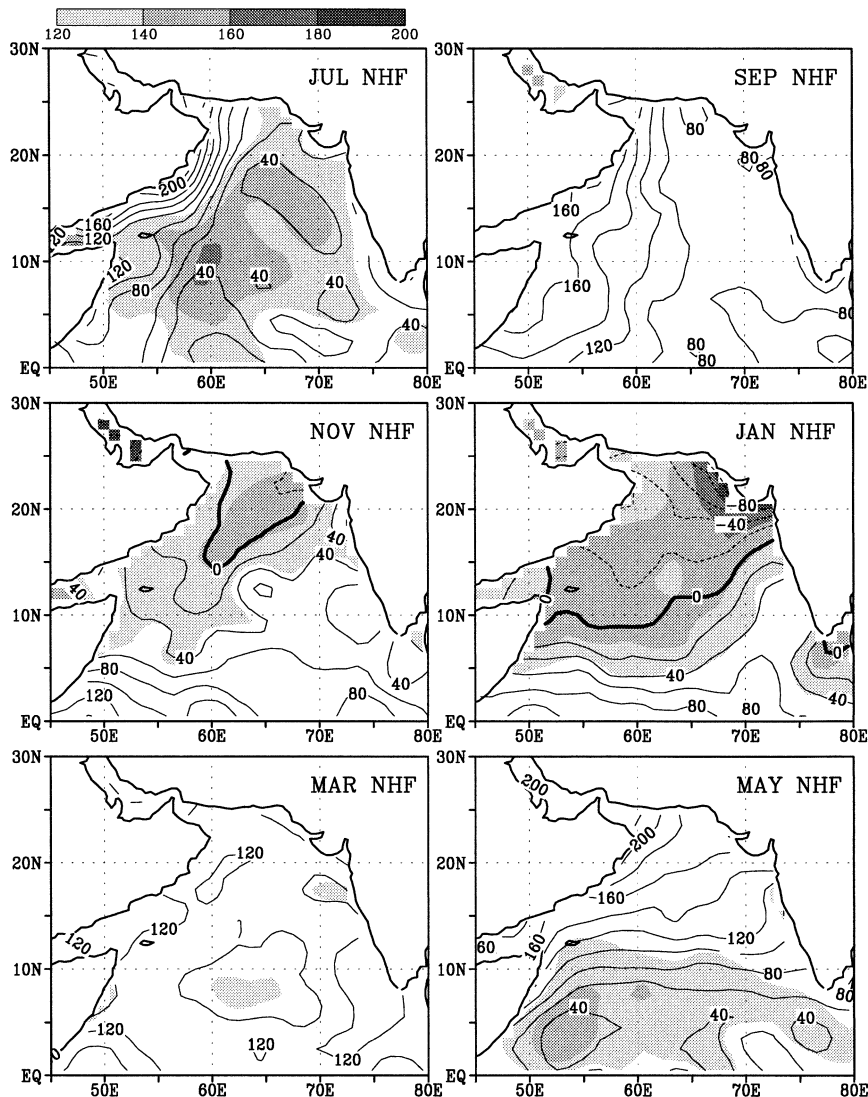
FIG. 3. Same as Fig. 2 but net heat flux observations from the SOC climatology (1980–93; Josey et al. 1999) in W m^{-2}. The contour interval is 20 W m^{-2}. Shading is provided for the SOC latent heat flux in W m^{-2} between 120 and 200 W m^{-2}. A remarkable agreement is revealed between the model and observed net heat flux during winter monsoon.

own fluxes of sensible, latent, and longwave radiation. In computing freshwater flux (evaporation minus precipitation) we used precipitation data from the SOC climatology (Josey et al. 1999) and evaporation is obtained from the model. See appendix B for details of air–sea heat flux computation.

3. Results

The model is applied to the Arabian Sea in the domain west of 80°E and north of the equator on a horizontal 1° × 1° grid. The vertical extent of the model is fixed to 200 m with 1-m intervals. The model integration is started in the month of April, during the transition period between the winter and summer monsoons when the

wind field is weakest and mixed layer is shallowest. Simulations were performed with the model initialized with observations of temperature and salinity taken from Levitus and Boyer (1994) and started from rest. The model is run for little more than a year with time step $\Delta T = 10$ s. Results presented in this paper are from the month of June to May.

a. Evolution of heat flux

An interesting feature of the heat budget of the Arabian Sea is that there is a net annual heat gain by the ocean (Hastenrath and Lamb 1979; Oberhuber 1988; da Silva et al. 1994; Josey et al. 1999). A large part of this heat energy, however, is confined in the upwelling re-
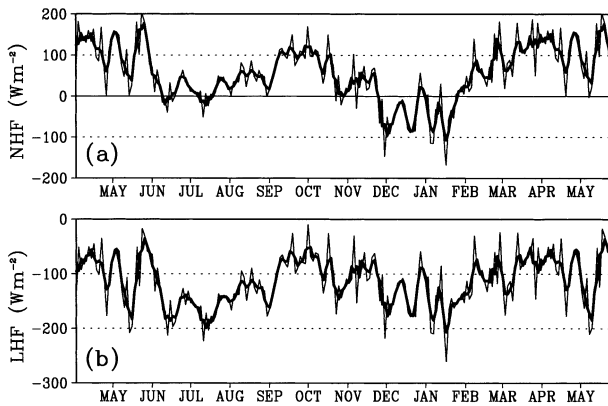
FIG. 4. Time series of the model-derived (a) net heat flux and (b) latent heat flux at the buoy observations location (61.5°E, 15.5°N). This is included for direct comparison with the Fig. 3 of Weller et al. (1998). Thick line is a 5-day moving average. The model captures the details of the early summer and winter monsoon net heat flux reasonably well.

gions (along the coasts of Somalia and Arabia) and decreases offshore. The relative large values of heat input in the western Arabian Sea can be attributed to increased solar heating due to lower cloudiness and reduced evaporative cooling (Hastenrath and Lamb 1979). The net heat flux at the ocean surface broadly determines the nature of stratification in the upper layers. A weakly (strongly) stratified upper layer can be maintained if

there is a net heat loss (gain) by the ocean under the weak prevailing winds.

Figure 2 shows the bimonthly net heat flux in W m^{-2} (July–May) obtained from the model. Shading is provided at 20 W m^{-2} intervals between 120 and 180 W m^{-2} for the model-derived latent heat flux. The annual march of net heat flux in the Arabian Sea undergoes two warming phases following the seasonal movement of the sun. The winter monsoon is characterized by a net heat loss from the ocean. With the onset of the summer monsoon, the northern Arabian Sea experiences a milder net heat loss from the ocean, which is dominated by contributions from the large latent heat release (>160 W m^{-2}). Heat uptake by the ocean along the coasts of Arabia and Oman is noteworthy (60–80 W m^{-2}). It is well known that the monsoon winds (Findlater Jet; Findlater 1969), which carry moist air from the south, dominate all the flux fields in the Arabian Sea during the summer monsoon. Reduced longwave radiation (due to cloudy skies) and latent heat flux (due to moist air) contribute to the weaker summertime heat losses. From early August to late September, the entire Arabian Sea gains heat from the atmosphere (60–80 W m^{-2}).

With the onset of northeast monsoon winds in the northern Arabian Sea, the net heat flux decreases rapidly from October (80 W m^{-2}) to November (20–40 W m^{-2}). The spectacular loss of heat in the northern Arabian Sea is dominated by the large latent heat release from the ocean as shown in Fig. 2. As expected, the latent heat
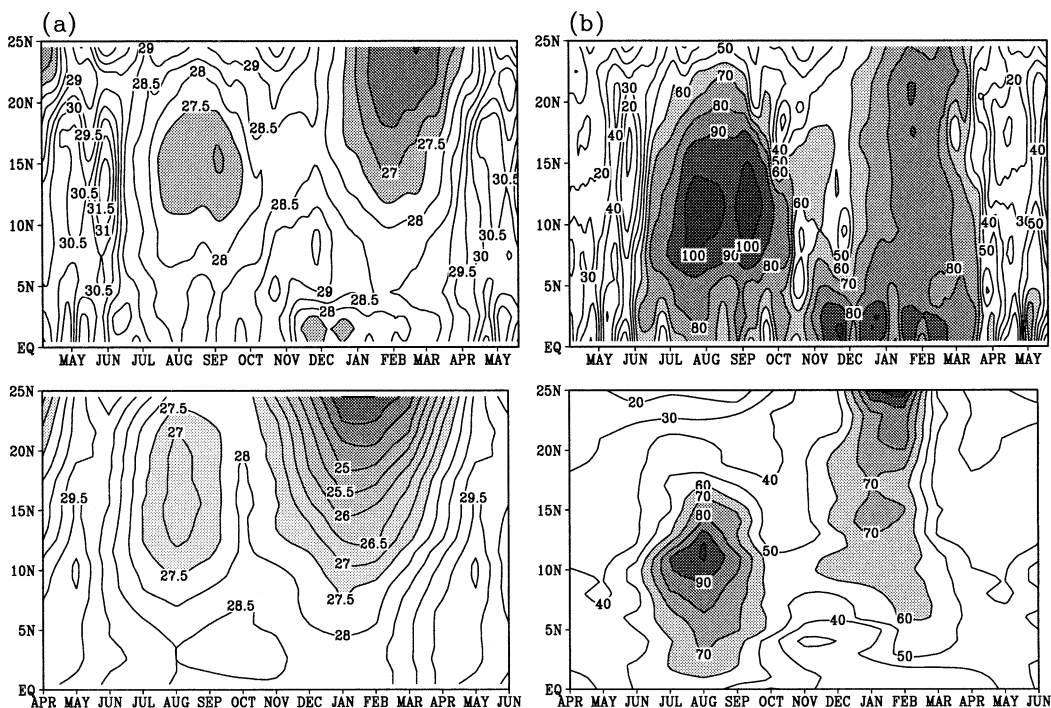

FIG. 5. Time–latitude plots of (a) SST and (b) MLD from the (top) model and the (bottom) corresponding observations along 64.5°E. A 10-day moving average is applied. Contour interval for SST (MLD) is 0.5°C (10 m). Shading is provided for the SST <27.5°C and MLD >60 m.

flux markedly increases from October (80 W m^{-2}) to December (140 W m^{-2}). Reduced solar insolation together with elevated latent heat release in the northern Arabian Sea result in a net heat loss of -40 W m^{-2} from the ocean. Part of this cooling is contributed by increased longwave radiation (70 W m^{-2}) due to lower cloudiness. By March, the ocean begins to gain heat (100 W m^{-2}) due to increasing solar radiation and reduced evaporation from the decreasing winds.

During transition periods, the ocean experiences a net heat gain on account of decreased latent heat (weak winds) together with increased solar insolation. During the spring season (March–May) the ocean receives 100–120 W m^{-2}, while it is around 60–80 W m^{-2} during fall (October) in the northern Arabian Sea. The difference in net heat flux during the transition periods can be attributed to the shift in solar insolation and relatively weaker winds during spring.

While several heat flux climatologies in the literature differ in the annual mean and during both monsoons (Weller et al. 1998), the SOC climatology for 1980–95 was found to best match the observations (see Weller et al. 1998; Lee et al. 2000). We use the air–sea heat flux from the SOC climatology for the period 1980–93 (Josey et al. 1999) for comparison with the model-derived heat flux fields. Bimonthly maps of SOC net heat flux (W m^{-2}) are shown in Fig. 3. Similar to model fields, shading is provided at 20 W m^{-2} intervals between 120 and 180 W m^{-2} for latent heat flux. A reasonable agreement between the model and observed net heat flux is found suggesting that the model has reproduced the basic evolution of the heat flux across the air–sea interface. In particular, net heat and latent heat fluxes during winter are close to the SOC climatology. Weller et al. (1998) reported a net heat loss of 45 W m^{-2} to the atmosphere during December and January, which qualifies our model value. Time series of net surface heat flux and latent heat flux from the model at 61.5°E, 15.5°N are depicted in Fig. 4. This is included for comparison with the time series data from the buoy location in the Arabian Sea (Weller et al. 1998, their Fig. 3). A remarkable outcome is that the model shows considerable skill in reproducing the net heat flux.

During July, the model net heat flux is lower than the SOC climatology by 40 W m^{-2} in the central Arabian Sea. The reason for this difference can be accounted for by the excessive latent cooling in the model (160–180 W m^{-2}). Weller et al. (1998) found that relative humidity plays an important role in modulating latent heat loss, resulting in weaker than anticipated summertime losses. However, a direct comparison of the buoy net and latent heat fluxes (Weller et al. 1998, their Fig. 3) with that of the model at 61.5°E, 15.5°N (Fig. 4) revealed a better agreement in July than with the SOC climatology, farther east and south. The net heat flux drops to close to zero in late July and the latent heat flux is -180 W m^{-2}. These values agree better with the buoy data than the SOC climatological heat fluxes.
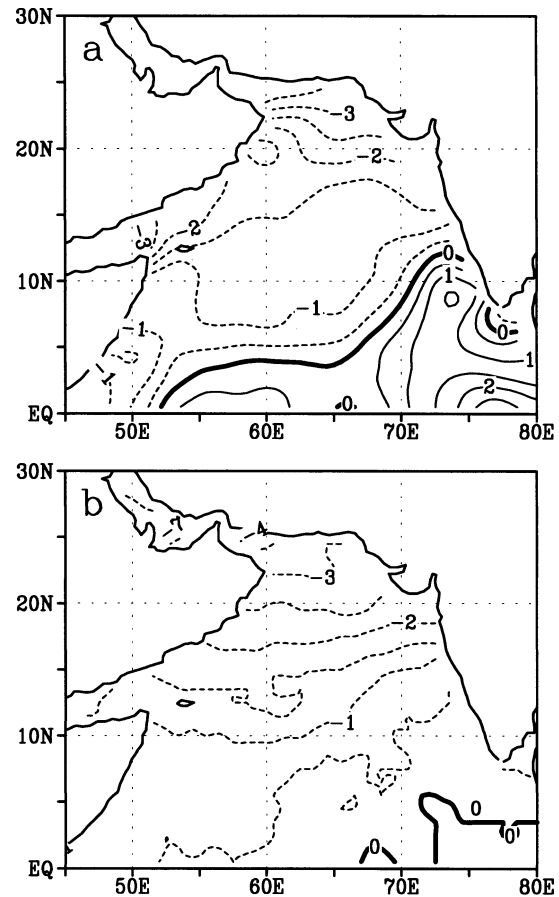

FIG. 6. The difference in SST between Nov and Feb (SST$_{\text{Feb}}$ minus SST$_{\text{Nov}}$) from the (a) model and (b) observed SST. The contour interval is 0.5°C. Note that the rate of cooling in the model and observed SST agrees well in the northern Arabian Sea.

It is also worth mentioning that the model-derived net heat flux during July is in better agreement with the climatological estimates from the Comprehensive Ocean–Atmosphere Data Set 1994 (da Silva et al. 1994) and model net heat flux (McCreary et al. 1993), which both indicate a mild heat loss. From early August, the entire Arabian Sea gains heat from the atmosphere, in agreement with the SOC climatology. While the model is able to represent the heat flux in the interior of the Arabian Sea, it failed to reproduce that along the upwelling regions (off Somalia, Arabia, and Oman) due to lack of upwelling and advective fields in the 1D model. The large difference in heat flux between the model and observations during summer in the upwelling regions can be attributed to relatively large sensible heat flux in the model due to difference in model SST and air temperature (see below).

b. Evolution of SST and MLD

In Fig. 5 we show smoothed (10-day running average) time series of the seasonal cycles of SST and MLD along
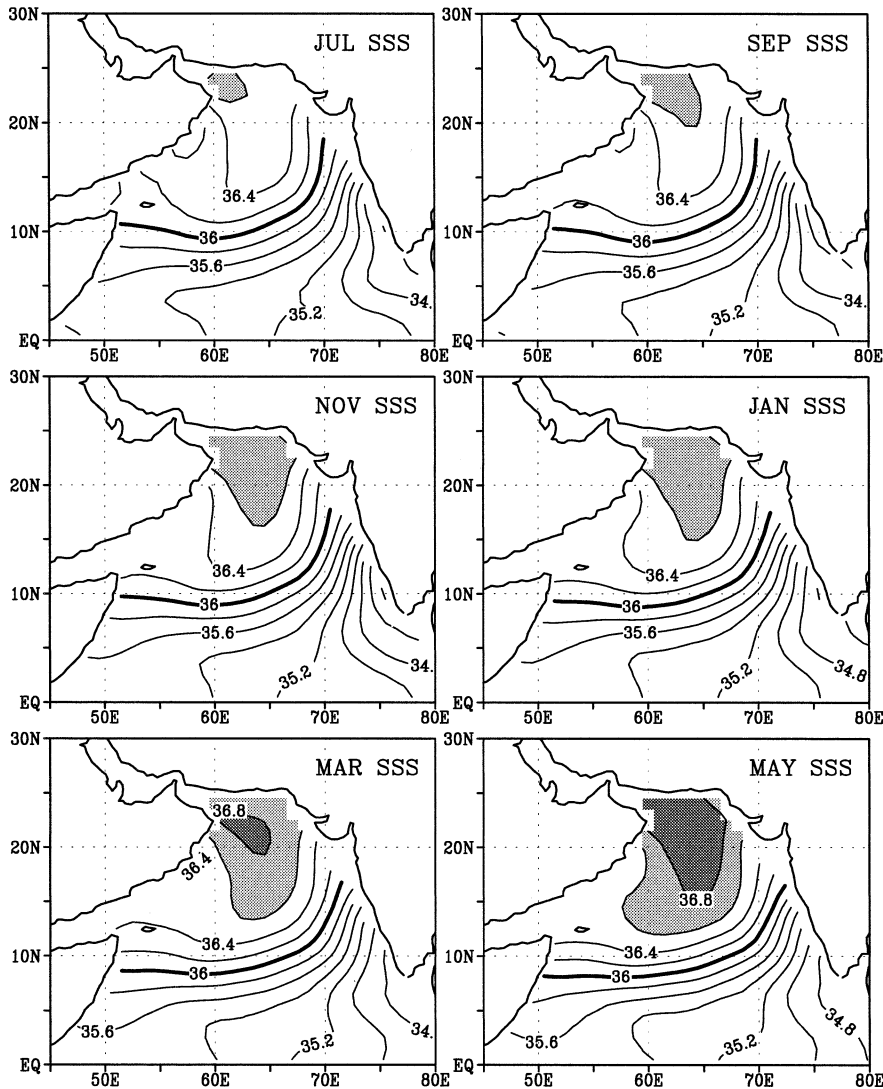
Fig. 7. Bimonthly maps of sea surface salinity (SSS) in psu from the model depicting the evolution of the Arabian Sea High Salinity Water mass (ASHSW). Shading is provided at 0.2 psu intervals from 36.6 psu to demarcate the newly formed ASHSW. The evolution of ASHSW is in general accord with the observations of Prasanna Kumar and Prasad (1999).

a meridional section 64.5°E (top panels) and the corresponding observed fields (bottom panels). In accordance with the net heat flux, seasonal cycles of SST and MLD are dominated by strong semiannual variability: two cooling (deep MLD) and two warming phases (shallow MLD). With the onset of the summer monsoon the wind stress increases (6.0 dyn cm^{-2}; Rao et al. 1989) in the Arabian Sea. The decrease of SST to 27.5°C during summer could be attributed to wind-driven vertical mixing. The turbulent shear stress acting on the mean velocity overwhelms the buoyancy forcing leading to enhanced vertical mixing. Bauer et al. (1991) proposed that Ekman pumping is the dominant mechanism governing the mixed layer response to the summer monsoon. Thus, open-ocean upwelling to the north of the Findlater Jet and downwelling to the south are

used to explain the observed cross-basin contrasts in mixed layer depth. In recent studies, however, Lee et al. (2000) and Fischer (2000) suggested that the strong, steady winds of the summer monsoon drive significant mixed layer deepening through turbulent mixing. Wind-driven turbulent mixing overwhelms the deepening due to Ekman pumping, though both processes contribute to additional deepening between July and August. Model mixed layer (100 m) also indicates that wind-driven vertical mixing is the dominant mechanism in establishing deep mixed layer in the central Arabian Sea during summer monsoon.

The second cooling phase of the annual cycle in SST begins with the onset of the northeast monsoon winds in the Arabian Sea from November to February. The wind stress gradually increases from north to south at-
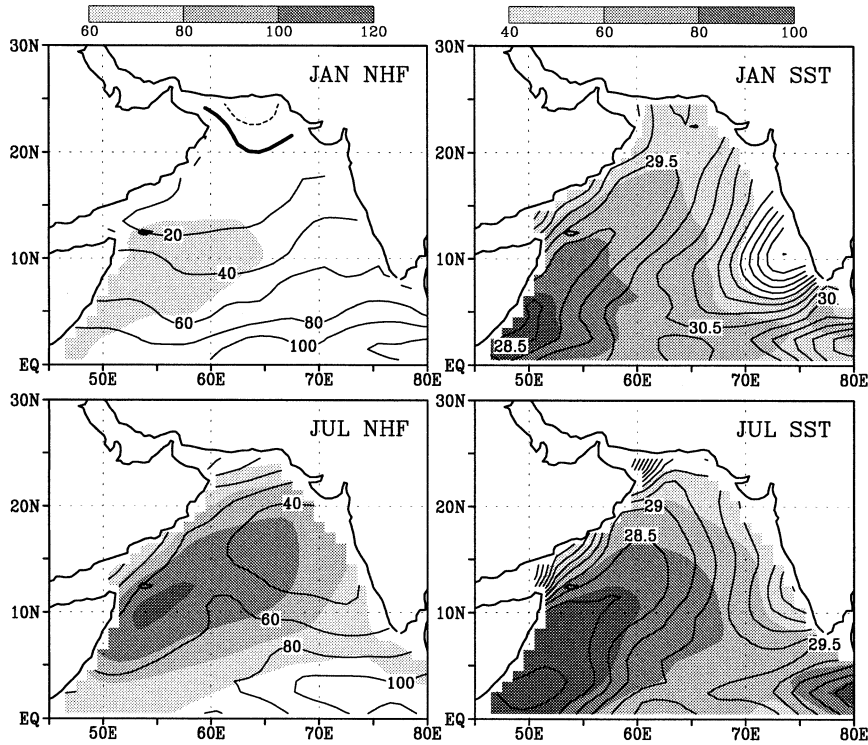
FIG. 8. (left) Monthly mean net heat flux and (right) SST during (top) Jan and (bottom) Jul from a test run keeping the relative humidity 90%. Contour interval is 20 W m^{-2} for net heat flux and 0.5°C for SST. (left) Shaded region is the model latent heat flux (W m^{-2}) greater than 60 W m^{-2} with intervals of 20, and (right) MLD greater than 40 m. There is a marked difference in net heat flux and SST during Jan from that of the main run (Figs. 2 and 3) indicating the role of humidity in the wintertime cooling.

taining 1 dyn cm^{-2} off Somalia region (Rao et al. 1989). However, in contrast to summer monsoon, the maximum cooling occurs in the northern Arabian Sea where the wind is relatively weak. Between November and February, SST decreases at a rate of 1°C per month (<26.5) in the northern Arabian Sea. To demonstrate this, we

FIG. 9. Time–latitude plot of specific humidity (SH) in gm kg^{-1} along 64.5°E from the SOC climatology (Josey et al. 1999). The SH less than 17 gm kg^{-1} is shaded. The SH drops from 18 gm kg^{-1} in Sep to 12 gm kg^{-1} in Jan indicating the presence of dry air from the north.

plot the difference in the model as well as observed SST field (February SST minus November SST) in Figs. 6a,b. The rate of cooling is substantial and quite comparable to the observed cooling, departing by less than 0.5°C and indicating that winter cooling is fairly well captured in the model. As a result of high evaporative cooling the surface buoyancy flux increases considerably. The turbulent energy production due to surface buoyancy flux overwhelms that due to shear stress at the surface in the northern Arabian Sea. This decreases the vertical stability of the water column causing increased vertical mixing resulting in downward fluxes of heat and momentum by convective overturning. As a consequence, the mixed layer deepens to 80 depth. Thus, weaker stratification (due to negative buoyancy) at the surface and subsequent vertical mixing result in a deep mixed layer and cool SST during winter.

During the transition periods (March–May, October–November), the increased solar heating together with reduced evaporative cooling (due to weak wind) produces strongly stratified upper layer (large Richardson number). This along with weak shear stress production at the surface (weak surface current) restricts the turbulent vertical mixing to a depth of about 20–40 m while the SST increases to 30°C.
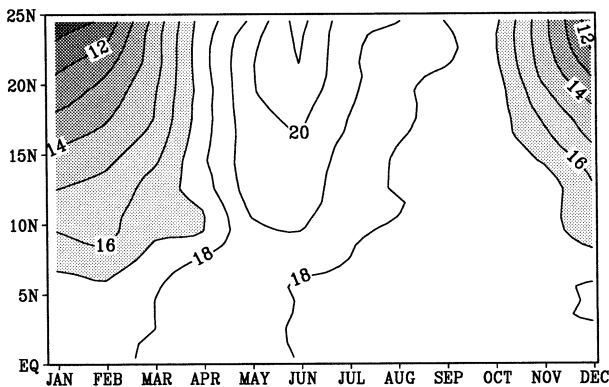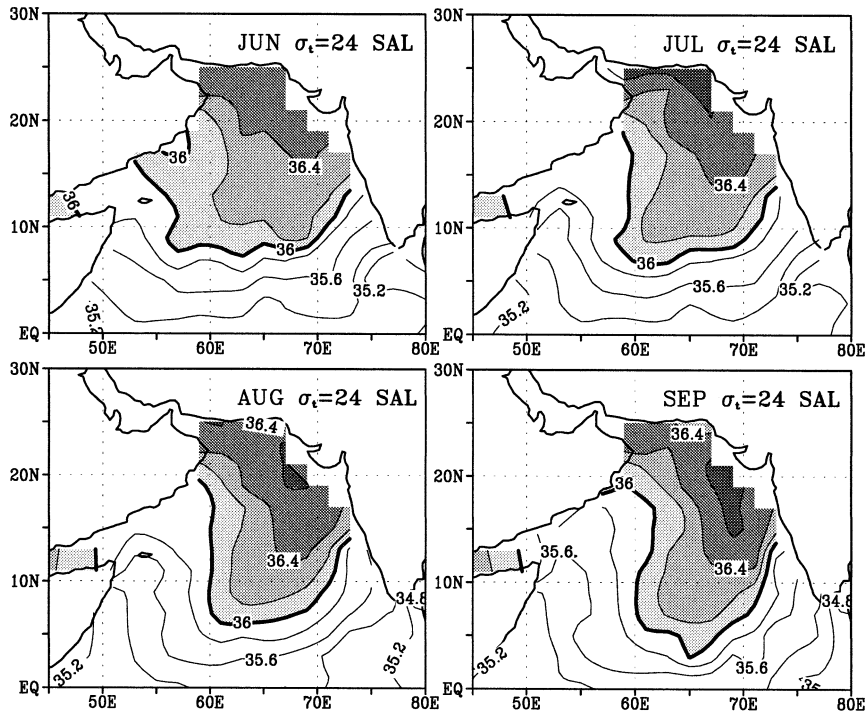
FIG. 10. Distribution of salinity on the isopycnal surface $\sigma_t = 24$ from Jun through Sep. The contour interval is 0.2 psu. Salinity values greater than 36.0 psu are shaded. The northward current along the coast of Arabia pushes the core northward, at the same time ASHSW starts spreading southward along the eastern Arabian Sea.

The model-simulated MLD and SST (SOC; Josey et al. 1999) are compared with the observed fields in Fig. 5. The MLD is computed from the Levitus and Boyer (1994) temperature climatology. MLD is taken as the depth at which the temperature is less than 1°C from the surface. Despite a warm SST in winter, the model exhibits considerable skill in simulating the SSTs, agreeing to within 1°C south of 15°N, along 64.5°E. The temporal variations in MLD and SST are fairly well reproduced in the model. In agreement with the observations, the modeled MLD is deep during both summer and winter monsoons. Model SST is 0.5°C higher than that from the SOC climatology SST at the peak of the summer monsoon. The difference in SST could be due to lateral advection of cooler upwelled waters (Lee et al. 2000). Although the SST during winter shows a decrease, the modeled SST is much higher than in the observations. A major part of difference in SST (which is more pronounced in the northernmost region) may have been caused by too much warming in the model during August–November. This warming slows down the winter cooling rate in the model from November through February. With the southwest monsoon winds in the northern Arabian Sea, instabilities of the northward-flowing coastal current along the coasts of Arabia and Oman carry cold upwelled water into the northern Arabian Sea causing reduction in SST in summer. A model with both horizontal advection and upwelling

mechanism could reasonably simulate the observed SST field such as that performed by McCreary and Kundu (1989). Although there is no mechanism in the model by which the excess heat can be removed effectively by horizontal advection, the model SST remains the same as the initial temperature a year later. This suggests that the momentum and heat fluxes at the surface locally balance the viscous dissipation in the open ocean.

c. Evolution of ASHSW

Figure 7 shows bimonthly mixed layer salinity in psu (July–May) depicting the evolution of ASHSW in the northern Arabian Sea. In order to demarcate the spatial extent of the newly formed ASHSW, shading is provided for the values greater than 36.6 psu. The distribution of salinity during July (36.4 psu) is apparently close to the initialization and persists until the end of September. A gradual increase in salinity by November is evident, offset by commencement of the NE trade winds in the northern Arabian Sea. The salinity progressively increases until the end of May, attaining a maximum value of 36.8 psu. This gives a rate of 0.1 psu per month. However, it is important to keep in mind that the model integration started from April, when the core salinity was 36.4 psu. The modeled salinity rapidly increases from March through May. The increased salinity by May could, in addition to being due to evaporation, benefit

from the increased stratification, making the surface layer response more sensitive to surface forcing. By May the ASHSW occupies large area in the northern Arabian Sea, which is in accordance with the observations. Despite the fact that upper-layer currents are weak during the winter, horizontal mixing due to the mesoscale eddy field could be nonnegligible. In winter, salinities with values 36.7 psu are observed at the core of the ASHSW (Prasanna Kumar and Prasad 1999) that are in approximate agreement with the modeled salinity. The resulting winter mixed layer depth deepens to 80 m and it broadly determines the volume of the ASHSW.

Time series data on temperature and salinity collected in the northern Arabian Sea (61.5°E, 15.5°N) from October 1994 through October 1995 also confirm similar features (Rudnick et al. 1997). Salinities with values 36.6 psu were noted in the observations during April–May in the upper 80 m. High mixed layer salinities of >36.8 psu were reported in an along-shelf section extending from the Gulf of Oman to Arabia during December [see Fig. 5 of Lee et al. (2000)]. Lee et al. (2000) also noted strong, surface-intensified along-shelf southward current with peak speeds >0.5 m s^{-1} in December and vanished by February, most likely driven by northeasterly winds. The high salinities found along the coast may be the result of southward advection of ASHSW from the Gulf of Oman. However, the velocity field in the northern Arabian Sea at two transects observed using shipboard acoustic Doppler current profiler by Flagg and Kim (1998) indicated that currents along the shelf regions are dominated by mesoscale eddies rather than an organized mean flow. During winter, they observed a surface-intensified jet called Ras al Hadd Jet, which rapidly changes direction in a timescale of weeks and flows against the prevailing winds. Thus, horizontal advection plays a significant role in the along-shelf transport/mixing of ASHSW during winter. Thus, along the shelf the response to the northeast monsoon cannot be explained by a locally forced 1D model. Nevertheless, the model has captured the essential features of seasonal evolution of the ASHSW fairly well and that is very much similar to that observed by Prasanna Kumar and Prasad (1999). South of 10°N, the modeled salinity distribution does not show any noticeable changes. This is expected, because the seasonally reversing equatorial current system broadly determines the salinity distribution in this region (discussed in the introduction).

d. Sensitivity to humidity

In order to identify and isolate the influence of forcing parameters that determine winter cooling and ASHSW formation, we have carried out a test run keeping the relative humidity 90% constant throughout a year. Figure 8 show the net heat flux (shaded region is the latent heat flux greater than 60 W m^{-2} with intervals of 20) and SST (shaded region is MLD from 40 m with intervals of 20) for January and July, respectively. The

difference in net heat flux in the high humidity run during January is substantial and accounts for a change of 60 W m^{-2} from the main run. The entire northern Arabian Sea experiences net heat gain by the ocean. On the other hand the net heat flux is of a different sign in July in the high humidity run, and closer to the SOC climatology. These differences, however, are principally due to the latent heat flux. The latent heat flux decreased markedly from the main run (140 W m^{-2}) by more than 50%. While there is an average of 1°C rise in SST from the main run during July, the January SST shows dramatic increase (3°C). Reduced evaporation due to increased humidity resulting in appreciable increases in the surface stratification, which restricts the penetration depth of convective mixing to about 40 m in winter. On the other hand, the resulting MLD (90 m) remains closer to that in the main run during July, suggesting that wind-driven turbulent mixing is the dominant mechanism governing deep MLD in the central Arabian Sea.

4. Discussion

We reported heat flux, SST, and MLD fields from a 1D model that are pertinent to the mechanism of wintertime water mass formation in the northern Arabian Sea. Modeled heat flux and MLD are in reasonable agreement with observed values (Josey et al. 1999; da Silva et al. 1994; Weller et al. 1998). The modeled SST during winter, however, departs significantly from the observed value principally due to the excess warming from summer to fall. This may be caused by the lack of advective field in the model. The advection of cold upwelled water along the coasts of Arabia and Oman into the northern Arabian Sea during summer causes a reduction in SST. Examination of these fields clearly indicated that while summer monsoon winds dominate all the flux fields in the Arabian Sea, the large latent heat release during a relatively weak wind regime account for the net heat loss from the ocean during winter. The reason for elevated latent heat release in the northern Arabian Sea can be delineated from Fig. 9 showing specific humidity (SH, SOC 1980–93) along 64.5°E. As expected, there is significant variability in SH from summer to winter. The SH drastically drops from 18 gm kg^{-1} in September to <12 gm kg^{-1} during January in the northern Arabian Sea manifesting presence of cool and dry air emanating from the north. This results in greater evaporation of water vapor from the ocean releasing the latent heat energy at the surface. Recall from the preceding discussion of the role of humidity in determining the net heat flux in the northern Arabian Sea during winter.

Thus, enhanced evaporation in conjunction with reduced solar radiation leads to a net heat loss (−40 W m^{-2}) in the northern Arabian Sea during winter. The production of turbulent energy due to buoyancy forcing dominates shear stress acting on the mean velocity. Increasing salinity and decreasing temperature at the sur-

face increases surface density. When the surface water becomes denser, it tends to sink and mixes the water below (80 m). This results in convective formation of the ASHSW. Despite the fact that the upper-layer currents are weak during the winter, horizontal mixing due to mesoscale eddy field could be nonnegligible.

Since we have ignored advection and lateral mixing in the simulation, it is important to investigate whether such a process is detrimental to ASHSW formation especially in the northern Arabian Sea during winter. The prevailing northeast trade winds in this region give rise to a weak southwest-flowing current (Cutler and Swallow 1984). In December, alongshelf flow is southward along the coast of Oman (sections A–D of Lee et al. 2000). Flagg and Kim (1998) indicated that alongshelf currents in the northern Arabian Sea are dominated by mesoscale eddies of timescales of a few weeks. These eddy-induced currents of variable direction often directed against the wind may transport or mix ASHSW with the ambient water along these regions. There is a narrow but weak northward geostrophic current flowing against the winds along the coast of Arabia during winter (Hastenrath and Greischar 1991). Its impacts on ASHSW formation is, however, rather minimal. The advection of low salinity water from the coast of Arabia does not yield a significant mixing during the ASHSW formation period. The intrusion of Bay of Bengal low salinity water carried by the WICC is unlikely because the current is weak and confined to south of 20°N in winter. It therefore seems reasonable to assume that advection of low salinity water carried by the coastal currents (October–May) into the northern Arabian Sea plays a negligible role in the formation of ASHSW. Nevertheless, a small degree of horizontal eddy mixing with the ambient waters cannot be dismissed particularly in the coastal regions.

Having discussed the formation mechanism, let us now examine how the newly formed water is being renewed from the source region in order to maintain salt balance in the basin and what currents accomplish this replacement. The southwest monsoon circulation is expected to play an important role in transporting this high salinity water into the equatorial region. To demonstrate this, we plot salinity on $\sigma_t = 24.0$ surface (representing the ASHSW core salinity located between 0 and 100 m depth) utilizing hydrographic data from the Levitus and Boyer (1994) for the southwest monsoon period (Fig. 10). As expected, the northward current along the coast of Arabia and Oman pushes ASHSW core northward. At the same time, ASHSW starts spreading southward along the eastern half of the Arabian Sea. By October, the whole newly formed ASHSW is replaced with water from the coast of Arabia and Oman. Thus, the presence of relatively cold and low salinity water (36.3 psu) in the northern Arabian Sea during late southwest monsoon period is expected to be advected from the upwelled regions. By early November, the ASHSW begins to form in the northern Arabian

Sea. A model with advection would be required to study in detail the spreading of ASHSW from the source region and its influence on surface circulation and horizontal mixing.

5. Summary and conclusions

Using a one-dimensional second-order level 2 turbulent closure model, we have demonstrated the seasonal evolution of the Arabian Sea high salinity water mass in the northern Arabian Sea during winter. The model exhibits considerable skill in reproducing the characteristics of water mass and surface fluxes that are responsible for the formation of ASHSW. The strong, steady winds of the summer monsoon are responsible for enhanced turbulent mixing, the dominant mechanism governing deep mixed layers and reduced SSTs, while very little is known about winter cooling in the northern Arabian Sea. In summer, the turbulent shear stress acting on the mean velocity shear is the source of turbulent energy at the base of the mixed layer. Enhanced evaporation (due to weak wind but dry air) together with reduced solar insolation lead to a net heat loss during winter. This suggests that it is the buoyancy instability associated with the turbulent heat loss exceeding the radiative heat gain at the surface that is responsible for the deep penetration of MLD and convective formation of ASHSW during winter. Weaker winds, strong near-surface stratification, and weaker shear stress during the transition periods (March–May, October) account for shallow mixed layer and high SST.

The formation of ASHSW at a rate of 0.1 psu per month persists until April. During April–May the ASHSW occupies a large area in the northern Arabian Sea in accordance with observations. The seasonal evolution of ASHSW is in good agreement with that observed by Prasanna Kumar and Prasad (1999) and limited in situ observations. The volume of the ASHSW formation can be largely approximated to the mixed layer depth during winter. While horizontal mixing due to mesoscale eddy field could be an important mechanism for ASHSW spreading during winter, the southwest monsoon circulation appears to transport ASHSW, maintaining the salt balance in the basin. The model also indicates the role of humidity in determining winter cooling and formation of ASHSW. By increasing humidity to 90% in the model, we have found large difference in net heat flux and SST in the northern Arabian Sea during winter monsoon. The significant differences in heat budget emphasize the necessity of improving the accuracy of humidity measurements in the northern Arabian Sea.

APPENDIX A

Model Equations

The q^2 is twice the turbulent kinetic energy,

$$q^2 = B_1 l^2 S_m \left[\left(\frac{\partial U}{\partial z} \right)^2 + \left(\frac{\partial V}{\partial z} \right)^2 \right] (1 - R_f), \quad (A1)$$

where the flux Richardson number R_f is

$$R_f = \frac{S_h}{S_m} \frac{\left(\beta_T \frac{\partial T}{\partial z} + \beta_S \frac{\partial S}{\partial z} \right) g}{\left(\frac{\partial U}{\partial z} \right)^2 + \left(\frac{\partial V}{\partial z} \right)^2}. \quad (A2)$$

The thermal and haline expansion coefficients β_T and β_S are

$$\beta_T = \{[1.3 - 0.025(S - 30)]T$$
$$+ [3.3 + 0.325(S - 30)]\} \times 10^{-5} \quad (A3a)$$

$$\beta_S = -76 \times 10^{-5}, \quad (A3b)$$

and $g = 9.8 \text{ m s}^{-2}$ is the gravitational acceleration. The mixing length l is

$$l = \frac{-kz}{1 - kz/l_0}, \quad (A4)$$

where k is the von Kármán constant ($k = 0.4$) and the asymptotic mixing length l_o is determined from

$$l_o = \frac{\alpha \int_{-\infty}^{0} |z| q \, dz}{\int_{-\infty}^{0} q \, dz}. \quad (A5)$$

The stability factors S_h and S_m are

$$S_h = 3A_2 \frac{\gamma_1 - (\gamma_1 + \gamma_2)R_f}{1 - R_f} \quad (A6a)$$

$$S_m = S_h \frac{A_1}{A_2} \frac{B_1(\gamma_1 - C) - [B_1(\gamma_1 - C) + (6A_1 + 3A_2)]R_f}{B_1 \gamma_1 - [B_1(\gamma_1 + \gamma_2) - 3A_1]R_f}$$

$$\gamma_1 = \frac{1}{3} - \frac{2A_1}{B_1}; \qquad \gamma_2 = \frac{B_2 + 6A_1}{B_1}$$

$$R_f = R_c = \frac{\gamma_1}{(\gamma_1 + \gamma_2)} = 0.19$$

$$S_{ho} = 3A_2 \qquad (S_h \text{ when } R_f = 0)$$

$$S_{mo} = S_{ho} A_1 \frac{(\gamma_1 - C)}{(A_2 \gamma_1)} \quad (S_m \text{ when } R_f = 0). \quad (A6b)$$

The constants $(A_1, A_2, B_1, B_2, C) = (0.92, 0.74, 16.6, 10.1, 0.08)$ are taken from Mellor and Yamada (1982).

The constants were determined by matching solutions to laboratory experiments.

APPENDIX B

Air–Sea Heat Flux

The wind stress is calculated from

$$\tau = \rho_a C_D |\mathbf{V}| \mathbf{V}, \quad (B1)$$

where $\rho_a = 1.175 \text{ kg m}^{-3}$ is the density of air and $C_D = 2.8 \times 10^{-3}$. Such a high value of C_D is found to be necessary to simulate a minimum mixed layer of 20 m in the Arabian Sea.

The sensible and latent heat flux is calculated from the bulk formula

$$Q_s = \rho_a C_p C_s |\mathbf{V}|(T_a - T_m) \quad (B2)$$

$$Q_l = \rho_a C_l L |\mathbf{V}|(q_a - q_m), \quad (B3)$$

where $C_p = 1004 \text{ Jkg}^{-1}\,°C$ is the specific heat of air, C_s and C_l are empirical coefficients, $L = 2.44 \times 10^6$ Jkg^{-1} is the latent heat of evaporation, q_m is the saturation specific humidity, q_a is the specific humidity, which is a product of humidity h_m and q_m; that is, $q_a = h_m q_m$. Thus

$$Q_l = \rho_a C_l L |\mathbf{V}|(1 - h_m)q_m, \quad (B4)$$

where q_m is computed using a polynomial approximation as a function of temperature (Murray 1967),

$$q_m = 4.8 \times 10^{-3} \, 10^{7.5(T_m-273)/(T_m-36)}. \quad (B5)$$

The longwave radiation (Budyko 1974) is calculated

$$Q_b = \delta \sigma T_a^3 [0.154(1 - c_1 C)T_a + 4(T_m - T_a)], \quad (B6)$$

where δ is the emissivity of the sea surface (0.97), σ is the Stefan–Boltzman constant, c_1 is cloud coefficient (0.55), C is the fractional cloudiness, T_a is the air temperature, and T_m is the temperature in the mixed layer.

REFERENCES

Bauer, S., G. L. Hitchcock, and D. B. Olson, 1991: Influence of monsoonally forced Ekman dynamics of upper surface layer depth and phytoplankton biomass distribution in the Arabian Sea. *Deep-Sea Res.,* **38A,** 531–553.
Budyko, M. I., 1974: *Climate and Life.* Academic Press, 508 pp.
Cutler, A. N., and S. C. Swallow, 1984: Surface currents of the Indian Ocean (to 25°S, 100°E). Compiled from historical data archived by The Met Office, Institute of Oceanographic Sciences, Rep. 187, Godalming, United Kingdom, 8 pp. and 36 charts.
da Silva, A. M., C. C. Young, and S. Levitus, 1994: *Algorithms and Procedures.* Vol. 1, *Atlas of Surface Marine Data 1994, NOAA Atlas NESDIS,* 83 pp.
Findlater, J., 1969: A major low-level air current near the Indian Ocean during the northern summer. *Quart. J. Roy. Meteor. Soc.,* **95,** 362–380.
Fischer, A. S., 2000: The upper ocean response to the monsoon in the Arabian Sea. Ph.D. thesis, Massachusetts Institute of Technology/Woods Hole Oceanographic Institute, 222 pp.
Flagg, C. N., and H.-S. Kim, 1998: Upper ocean currents in the northern Arabian Sea from shipboard ADCP measurements col-

lected during the 1994–1996 U.S. JGOFS and ONR programs. *Deep-Sea Res. II,* **45,** 1917–1959.

Hasternrath, S., and P. J. Lamb, 1979: *Climatic Atlas of the Indian Ocean. Part 2: The Oceanic Heat Budget.* University of Wisconsin Press, 110 pp.

——, and L. Greischar, 1991: The monsoonal current regimes of the tropical Indian Ocean: Observed surface flow fields and their geostrophic and wind-driven component. *J. Geophys. Res.,* **96,** 12 619–12 633.

Ikeda, M., 1986: A mixed layer beneath melting sea ice in the marginal ice zone using a one-dimensional turbulent closure model. *J. Geophys. Res.,* **91,** 5054–5060.

Josey, S., E. Kent, and P. Taylor, 1999: New insights into the ocean heat budget closure problem from analysis of the SOC air–sea flux climatology. *J. Climate,* **12,** 2856–2880.

Kraus, E. B., and J. S. Turner, 1967: A one-dimensional model of the seasonal thermocline. II: The general theory and its consequences. *Tellus,* **19,** 98–106.

Lee, C. M., B. H. Jones, K. H. Brink, and A. S. Fischer, 2000: The upper ocean response to monsoonal forcing in the Arabian Sea: Seasonal and spatial variability. *Deep-Sea Res. II,* **47,** 1177–1226.

Levitus, S., and T. P., Boyer, 1994: *Temperature.* Vol. 4, *World Ocean Atlas 1994,* NOAA Atlas NESDIS, 117 pp.

McCreary, J. P., and P. K. Kundu, 1989: A numerical investigation of sea surface temperature variability in the Arabian Sea. *J. Geophys. Res.,* **94,** 16 097–16 114.

——, ——, and R. L. Molinari, 1993: A numerical investigation of the dynamics, thermodynamics, and mixed layer processes in the Indian Ocean. *Progress in Oceanography,* Vol. 31, Pergamon Press, 181–244.

Mellor, G. L., and P. A. Durbin, 1975: The structure and dynamics of the ocean surface mixed layer. *J. Phys. Oceanogr.,* **5,** 718–728.

——, and T. Yamada, 1982: Development of a turbulent closure model for geophysical fluid problems. *Rev. Geophys.,* **20,** 851–875.

Molinari, R. L., J. Swallow, and J. F. Festa, 1986: Evolution of the near-surface thermal structure in the western Indian Ocean during FGGE, 1979. *J. Mar. Res.,* **44,** 739–763.

Morrison, J. M., 1997: Inter-monsoonal changes in the T–S properties of the near-surface waters of the northern Arabian Sea. *Geophys. Res. Lett.,* **24,** 2553–2556.

Murray, F. W., 1967: On the computation of saturation vapor pressure. *J. Appl. Meteor.,* **6,** 203–204.

Oberhuber, J. M., 1988: An atlas based on COADS data set. Max-Planck-Institut für Meteorologie Tech. Rep. 15, 182 pp.

Prasanna Kumar, S., and T. G. Prasad, 1999: Formation and spreading of Arabian Sea high salinity water mass. *J. Geophys. Res.,* **104,** 1455–1464.

Rao, R. R., 1986: Cooling and deepening of the mixed layer in the central Arabian Sea during MONSOON-77: Observations and simulations. *Deep-Sea Res.,* **33,** 1413–1424.

——, and R. Sivakumar, 1999: On the possible mechanisms of the evolution of a mini-warm pool during the pre-summer monsoon season and the genesis of onset vortex in the south-eastern Arabian Sea. *Quart. J. Roy. Meteor. Soc.,* **125,** 787–809.

——, R. L. Molinari, and J. F. Festa, 1989: Evolution of the climatological near-surface thermal structure of the tropical Indian Ocean 1. Description of mean monthly mixed layer depth, sea surface temperature, surface current and surface meteorological fields. *J. Geophys. Res.,* **94,** 10 801–10 815.

Rochford, D. J., 1964: Salinity maxima in the upper 1000 m of the North Indian Ocean. *Aust. J. Mar. Freshwater Res.,* **15,** 1–24.

Rudnick, D. L., R. A. Weller, C. C. Eriksen, T. D. Dickey, J. Marra, and C. Langdon, 1997: Moored instruments weather Arabian Sea Monsoons, yield data. *Eos, Trans. Amer. Geophys. Union,* **78,** 120–121.

Shenoi, S. S. C., D. Shankar, and S. R. Shetye, 1999: On the sea surface temperature high in the Lakshadweep Sea before the onset of the southwest monsoon. *J. Geophys. Res.,* **104,** 15 703–15 712.

Sheyte, S. R., 1986: A model study of the seasonal cycle of the Arabian Sea surface temperature. *J. Mar. Res.,* **44,** 521–542.

——, A. D. Gouveia, S. S. C. Shenoi, G. S. Michael, D. Sunder, A. A. Almeida, and K. Sandanam, 1991: The coastal currents off western India during northeast monsoon. *Deep-Sea Res.,* **38A,** 1517–1529.

Weller, R. A., M. F. Baumgartner, S. A. Josey, A. S. Fischer, and J. C. Kindle, 1998: Atmospheric forcing in the Arabian Sea during 1994–1995: Observations and comparisons with climatology and models. *Deep-Sea Res. II,* **45,** 1961–1999.